Journal of Computational Applied Mechanics 2024, 55(4): 567-588

DOI: 10.22059/JCAMECH.2024.373245.988

RESEARCH PAPER

Thermal Radiation and Shape Factor Effects on Electro-magnetohydrodynamic Tri-hybrid Williamson Liquid Flow Around a Cylinder

Abdulkareem Saleh Hamarsheh[a,*] , Ehab A. El-sayed [b]

[a] *Department of Mathematics, College of Sciences and Humanities in Al-Kharj, Prince Sattam bin Abdulaziz University, Al-Kharj 11942, Saudi Arabia*

[b] *Department of Science and Engineering Mathematics, Faculty of Petroleum and Mining Engineering, Suez University, P.O.BOX 43221, Suez, Egypt*

Abstract

Industries such as film manufacturing and polymer solution processing benefit from the Williamson fluid model because it more accurately characterizes the behaviour of pseudo-plastic fluids by including maximum and minimum viscosities. This work presents a numerical simulation that investigates the thermal behaviour of tri-hybrid Williamson nanoliquid flow around a cylindrical surface. The primary focus of the study is to examine the influence of thermal radiation, electro-magnetohydrodynamic (EMHD), and the shape factor of nanomaterials on the physical quantities of energy transfer-related. Through the utilization of the hybrid linearization spectral method, the mathematical model that governs the problem is solved. The credibility and reliability of the obtained results are firmly established through verification against existing findings. The main results of this study reveal a remarkable decrease in heat transfer improvement for the tri-hybrid nanofluid as the Weissenberg number increases. The skin friction is shown to exhibit a clear increasing trend with the radiation coefficient, while the augmentation of the volume fraction factor or electrical factor demonstrates a discernible amelioration in velocity profiles. With increasing volume fraction, using Al_2O_3(hexahedron) - TiO_2(tetrahedron) - Cu(lamina) / H_2O raises the Nusselt number by 0.02 - 5% while decreasing skin friction by 1.3 - 9% compared with using Al_2O_3(sphere)-TiO_2(sphere)-Cu(sphere)/H_2O

Keywords: EMHD; Shape factor; Thermal radiation; Tri-hybrid nanoliquid; Williamson fluid.

1. Introduction

The Williamson fluid model is widely recognized as a prominent and influential framework for studying non-Newtonian fluids, particularly pseudo-plastic fluids. By incorporating both maximum and minimum viscosities, Williamson's [1] 1929 proposal and subsequent experimental investigations successfully capture the complex behaviour of these fluids. This inclusion of both maximum

* Corresponding author. *E-mail address:* a.hamarsheh@psau.edu.sa

and minimum viscosities enhances the accuracy of characterizing the behaviour of these fluids and contributes to the improvement of results. Additionally, it provides more accurate estimates of heat transfer rates and temperature distributions in many industrial and technical contexts due to its ability to effectively reflect the non-linear viscosity behaviour of pseudo-plastic fluids. Thus, the Williamson fluid model holds significant value in industries where pseudo-plastic fluids are used, such as in the processing of high-molecular-weight polymer solutions, photographic film manufacturing, and the extrusion of polymer sheets. Bilal et al. [2] demonstrated in their study about Williamson fluid moving across a cylinder under temperature stratification that the Williamson factor has an adverse association with the velocity profile. There is a negative trend in the skin friction coefficient towards escalating values of the Williamson factor. The energy transport through a Williamson nanoliquid flowing over a stretching cylinder subject to a chemical reaction and MHD effects was investigated by Ibrahim and Negera [3]. The Williamson factor was found to have a declining impact on velocity and a rising impact on temperature and concentration. Alwawi et al. [4] shed light on the energy transfer and flow characteristics of a Williamson hybrid nanofluid with an applied magnetic field. In accordance with their research, raising the Williamson factor results in a surging temperature and a reduction in velocity, the Nusselt number, and skin friction. Using a non-Fourier Cattaneo-Christov heat flux along with the Williamson model, Latha et al. [5] looked into MHD non-Newtonian flow and energy transport in a tri-hybrid nanoliquid. They discovered that a larger Williamson factor results in declining streamline magnitudes. Studies [6, 7] presented numerical simulations and parametric analyses of the Williamson hybrid nanoliquid flowing around spherical and cylindrical bodies.

As a major step forward in the field of heat transfer science, the ternary hybrid nanofluid offers a one-of-a-kind way to improve thermal conduction by combining three different nanoparticles in a way that works well together. This innovative fluidic composition uses the complex interplay of physicochemical properties that are unique to each nanoparticle, putting together a complex mix of thermal efficiency that goes beyond what is normally possible. In this unexplored frontier, the ternary hybrid nanofluid unveils a realm of unprecedented possibilities with far-reaching implications across diverse disciplines, spanning renewable energy systems, electronic cooling technologies, and aerospace engineering. As the scientific community embarks on this uncharted trajectory, the limitless potential of thermal engineering unfolds, promising revolutionary advancements that defy traditional paradigms and usher in an era of unparalleled scientific progress [8-11]. Numerical investigations focusing on tri-hybrid nanofluids have emerged as a critical area of research within the realm of heat transfer science. Mahmood et al. [12] investigated the time-dependent MHD flow of ternary hybrid nanoliquid over a spherical surface. Their numerical simulations revealed that the magnetic force and nanomaterial concentration exerted a positive impact on thermal distribution, but the unsteadiness and rotation parameters had the opposite effect. Tri-hybrid nanoliquids are able to carry energy at higher rates than both hybrid and mono-nanoliquids. Alwawi et al. [13] studied the extent of improvement in the flow characteristics of the magnetized micropolar liquid and the rate of energy transfer through the trihybrid nanomaterials. According to their outcomes, a higher magnetic factor value can limit the rate, velocity, and angular velocity of heat transmission. Using ternary hybrid nano-liquids allows for the greatest value of velocity, temperature, rate of heat transmission, and drag force. Mumtaz et al. [14] looked into the MHD flow of upgraded hybrid nanoliquid over a curved sheet in the presence of exponential heating and chemical reactions. According to the study, lowering the surface's curvature results in a reduction in drag force. A rise in the heat source's value and thermophoresis causes the rate of energy transmission to surge.

One key advantage of integrating magnetic and electric fields in the world of heat transfer is the ability to manipulate fluid motion by means of electromagnetic forces. The utilization of magnetic fields, commonly referred to as magnetohydrodynamics (MHD), has the capability to control fluid motion. The application of an electric field enables the utilization of electrohydrodynamics (EHD) processes, which in turn results in the augmentation of fluid motion and the amplification of heat transfer. The interaction between these disciplines facilitates meticulous manipulation of fluid flow patterns, velocities, and rates of heat transfer, hence facilitating the enhancement of heat transfer efficiency. Numerous numerical investigations have been devoted to combining the impacts of electric and magnetic fields. Hsiao [15]looked into how the EMHD Joule dissipation and mixed convection of a Maxwell liquid affect heat and mass transport. According to his findings, higher values of viscoelastic number, natural convection factor, and electric factor will result in a higher heat transport rate. Mehmood et al. [16] used the flux mathematical model to study the electromagnetohydrodynamic flow of alumina-ethylene glycol on a radiative stretching cylinder. Their results showed that drag force improves when electric and magnetic factors rise. The flow profiles reduce as the magnetic factor rises, while the thermal boundary layer profiles improve. The electric factor enhances both the flow and thermal profiles. Jakeer et al. [17] explored the impact of non-linear Darcy-Forchheimer on the transport of mono, hybrid, and tri-hybrid nanoliquids past a stretching sheet with thermal radiation, magnetic force, and an electric field. Their results confirmed that raising thermal radiation raises liquid temperature. Tri-hybrid nanoliquid has the greatest impact on the temperature profile.

The nanoparticle shape factor is crucial in the context of fluid-nanoparticle flows because it can substantially affect the transport characteristics of energy. When it comes to heat transfer, different shapes of nanoparticles will have different shape factors and, therefore, different transfer rates. Kumar et al. [18] confirmed that increasing the shape factor of the particles contributes to improving thermal conductivity. According to Sheikholeslami and Shehzad [19], platelet-shaped nanosolids transmit heat at a faster rate than nanosolids with spherical, cylindrical, or brick shapes. A numerical analysis conducted by Ghobadi and Hassankolaei [20]

revealed that lamina nanosolids influence the Nusselt number more than hexagonal nanosolids. Studies [21-23] have also conducted comparisons between various shapes of nanomaterials in terms of the efficiency of heat transport and the extent of their impact on flow characteristics. On the other hand, energy transfer in these flows is further aided by thermal radiation effects, which are subject to the laws of electromagnetic radiation and thermodynamics, in which heat transmission within a system can be affected by the presence of nanoparticles because of their ability to both emit and absorb radiation. Sheikholeslami et al.'s [24] analysis revealed the Nusselt number is an increasing function of the radiation factor. The findings of El-Kabeir et al. [25] validated that when the radiation factor becomes stronger, there is a corresponding rise in both drag force and the rate of energy transmission. Based on a numerical analysis conducted by Lone et al. [26], it was observed that the Nusselt number exhibited a significant increase when the radiation factor increased. Refer to these intriguing investigations [4, 6, 27]

The sources listed above indicate a research gap in the understanding of how thermal radiation and shape factors influence the flow behaviour of an EMHD tri-hybrid Williamson liquid around a cylinder. By incorporating thermal radiation and the shape factor of nanosolids into the analysis, it can gain insights into how this additional heat transfer mechanism affects the flow characteristics of the EMHD tri-hybrid Williamson liquid.

Following the dynamic aim and reasons, the present investigation has access to responses to the following research questions:

- What are the unique rheological characteristics that Williamson liquid will exhibit?
- What is the extent of improvements to the thermal features of the host Williamson fluid through the incorporation of trihybrid nanomaterials?
- What are the effects of magnetic force, electric force, and thermal radiation on the mechanism of energy transfer?
- How does the shape of nanoparticles affect the energy transportation process and flow characteristics of a Williamson liquid?

1. Mathematical description of thermophysical properties

The following formula determines the thermal conductivity of mono-nanofluids [28, 29]:

$$k_{NF} = k_{BF}\left(\frac{k_p + (m-1)k_F - (m-1)\Phi_p(k_F - k_p)}{k_p + (m-1)k_F + \Phi_p(k_F - k_p)}\right) \tag{1}$$

$m = 3/\eta$ represents the shape factor, and η represents the sphericity of the particle, which is calculated by finding the ratio between the surface area of the particle when it is in a spherical shape and the surface area of the particle in the other shape, taking into account that the volume of the particle in both shapes is equal. Table 1. provides the particles' shape used in the current investigation, along with their sphericity and shape factors.

Table 1: Sphericity and shape factor of nanomaterials [30, 31]

Shape of nanosolid	Hexahedron	Tetrahedron	Lamina	Sphere
Sphericity (η)	0.8060	0.7387	0.1857	1
Shape factor (m)	3.7221	4.0613	16.1576	3

The thermophysical properties of tri-hybrid nanofluid can be obtained via the following mathematical formulas, as described in [23, 32]:

$$\begin{aligned}
&\rho_{THNF} = \rho_1\Phi_1 + \rho_2\Phi_2 + \rho_3\Phi_3 + \left((1-\Phi)\rho_F\right),\\
&\left(\rho C_P\right)_{THNF} = \left(\rho C_P\right)_1\Phi_1 + \left(\rho C_P\right)_2\Phi_2 + \left(\rho C_P\right)_3\Phi_3 + \left((1-\Phi)\left(\rho C_P\right)_F\right),\\
&\beta_{THNF} = \beta_1\Phi_1 + \beta_2\Phi_2 + \beta_3\Phi_3 + \left((1-\Phi)\beta_F\right),\\
&\mu_{THNF} = \frac{\mu_F}{\left(1-\Phi_1\right)^{2.5}\left(1-\Phi_2\right)^{2.5}\left(1-\Phi_3\right)^{2.5}},\\
&\frac{k_{THNF}}{k_F} = \frac{k_{NF1}\Phi_1 + k_{NF2}\Phi_2 + k_{NF3}\Phi_3}{\Phi k_F},
\end{aligned} \tag{2}$$

$$\frac{\sigma_{NF}}{\sigma_F}=\frac{\sigma_1+2\sigma_F-2\Phi_1\left(\sigma_F-\sigma_1\right)}{\sigma_1+2\sigma_F+\Phi_1\left(\sigma_F-\sigma_1\right)},$$
$$\frac{\sigma_{HNF}}{\sigma_{NF}}=\frac{\sigma_2+2\sigma_{NF}-2\Phi_2\left(\sigma_{NF}-\sigma_2\right)}{\sigma_2+2\sigma_{NF}+\Phi_2\left(\sigma_{NF}-\sigma_2\right)},$$
$$\frac{\sigma_{THNF}}{\sigma_{HNF}}=\frac{\sigma_3+2\sigma_{HNF}-2\Phi_3\left(\sigma_{HNF}-\sigma_3\right)}{\sigma_3+2\sigma_{HNF}+\Phi_3\left(\sigma_{HNF}-\sigma_3\right)}.$$

The subscriptions 1 denotes Al_2O_3, 2 denotes Cu, and 3 denotes TiO_2. $\Phi=\Phi_1+\Phi_2+\Phi_3$ represents the combined volume fraction of nanomaterials. Both the host fluid and the nanosolids used in this investigation have their thermophysical features listed in Table 2.

Table 2: Thermophysical properties of base liquid and nanomaterials [33-37]

Thermo-Physical feature	H_2O	Al_2O_3	Cu	TiO_2
ρc_p *(J/kg K)*	4179	٧73	385	686.2
β *×10⁻⁵(K⁻¹)*	21	0.85	1.67	0.9
ρ (kg/m³)	997.1	3970	8933	4250
k (W/m K)	0.613	۴۰	401	8.9538
σ(1/Ωm)	0.05	1×10^{-10}	$5.96\text{x}10^{7}$	6.27×10^{-5}
Pr	6.1723	…	…	…

3. Constructing mathematical model

A steady laminar flow of tri-hybrid Williamson nanoliquid over a cylindrical surface is considered, along with the following assumptions:

- The presence of magnetic and electric fields that are transverse to the direction of flow.
- The presence of thermal radiation.
- Heat transfer occurs through free convection.
- The temperature of the surrounding medium T_∞ is higher than the temperature of the cylindrical surface T_w.

Fig 1 further clarifies previous assumptions. Additionally, let's also suppose that *x* is the first dimension that measures along the circumference of the cylindrical surface and that *y* is the second dimension that is perpendicular to *x*.

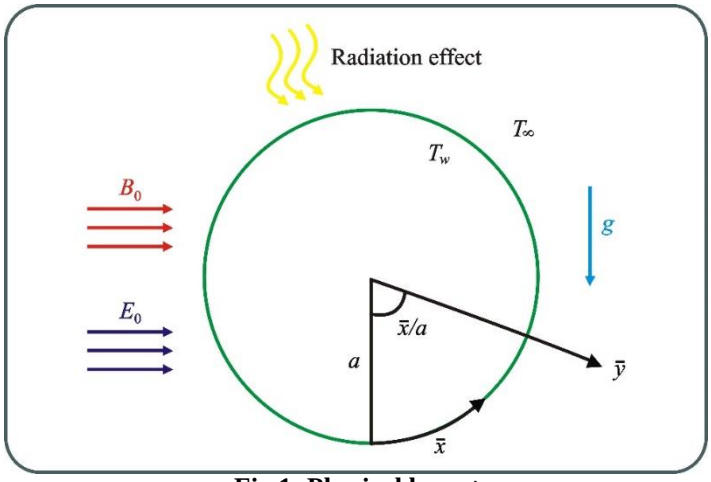

Fig 1: Physical layout

The aforementioned assumptions yield the following mathematical formulations (see [6, 17, 38]):

$$\frac{\partial \overline{v}}{\partial \overline{x}}+\frac{\partial \overline{w}}{\partial \overline{y}}=0, \tag{3}$$

$$\rho_{THNF}\left(\overline{v}\frac{\partial \overline{v}}{\partial \overline{x}}+\overline{w}\frac{\partial \overline{v}}{\partial \overline{y}}\right)=\sqrt{2}\mu_{THNF}\Gamma\left(\frac{\partial^2 \overline{v}}{\partial \overline{y}^2}\frac{\partial \overline{v}}{\partial \overline{y}}\right)+\mu_{THNF}\frac{\partial^2 \overline{v}}{\partial \overline{y}^2} +\beta_{THNF}\rho_{THNF}g\left(T-T_\infty\right)\sin\frac{\overline{x}}{a}-\sigma_{THNF}\left(B_0^2\overline{v}-E_0B_0\right), \tag{4}$$

$$\overline{v}\frac{\partial T}{\partial \overline{x}}+\overline{w}\frac{\partial T}{\partial \overline{y}}=\alpha_{THNF}\frac{\partial^2 T}{\partial \overline{y}^2}-\frac{1}{\left(\rho C_P\right)_{THNF}}\frac{\partial T}{\partial \overline{y}}\frac{\partial q_r}{\partial \overline{y}} \tag{5}$$

Under the following specified boundary conditions:

$$\begin{aligned}&\overline{v}=\overline{w}=0,\ T=T_w \text{ at } \overline{y}=0,\\ &\overline{w}\to 0, T\to T_\infty \text{ as } \overline{y}\to\infty.\end{aligned} \tag{6}$$

$q_r=-\dfrac{4\tau^*}{3\gamma^*}\left(\dfrac{\partial T^4}{\partial \overline{y}}\right)_{\overline{y}=0}$ represents the Rosseland approximation, where $T^4\cong 4T_\infty^3T-3T_\infty^4$. τ^* and γ^* represent the Stefan–Boltzmann and mean absorption, respectively. The dimensionless process entails introducing the following transformations:

$$x=\frac{\overline{x}}{a},\ y=\frac{\overline{y}Gr^{1/4}}{a},\ \theta=\frac{T-T_\infty}{T_w-T_\infty},\ v=\frac{a\,\overline{v}\,Gr^{-1/2}}{v_F},\ w=\frac{a\,\overline{w}Gr^{-1/4}}{v_F}. \tag{7}$$

$q_r=\dfrac{ga^3\beta_F\left(T-T_\infty\right)}{v_F^2}$ represents the Grashof number. Using transformations (7) results in the following dimensionless mathematical formations:

$$\frac{\partial v}{\partial x}+\frac{\partial w}{\partial y}=0, \tag{8}$$

$$v\frac{\partial v}{\partial x}+w\frac{\partial v}{\partial y}=\frac{\rho_F}{\rho_{THNF}}\frac{\mu_{THNF}}{\mu_F}We\left(\frac{\partial^2 v}{\partial y^2}\frac{\partial v}{\partial y}\right)+\frac{\rho_F}{\rho_{THNF}}\frac{\mu_{THNF}}{\mu_F}\frac{\partial^2 v}{\partial y^2} +\frac{\beta_{THNF}}{\beta_F}\theta\sin x-\frac{\rho_F}{\rho_{THNF}}\frac{\sigma_{THNF}}{\sigma_F}M\left(v-E\right), \tag{9}$$

$$v\frac{\partial \theta}{\partial x}+w\frac{\partial \theta}{\partial y}=\frac{1}{\Pr}\frac{\left(\rho c_p\right)_F}{\left(\rho c_p\right)_{THNF}}\left(\frac{k_{THNF}}{k_F}+\frac{4}{3}L\right)\frac{\partial^2\theta}{\partial y^2}. \tag{10}$$

Subject to:

$$\begin{aligned}&v=w=0,\ \theta=1 \text{ at } y=0,\\ &w\to 0,\ \theta\to 0 \text{ as } y\to\infty.\end{aligned} \tag{11}$$

where $\Pr = \frac{\nu_F}{\alpha_F}, We = \frac{\sqrt{2}\Gamma Gr^{3/4}\nu_F}{a^2}, M = \frac{\sigma_F a^2 B_0^2 Gr^{-1/2}}{\rho_F \nu_F}$, $L = \frac{4\sigma^* T_\infty^3}{k_F 4k^*}$, and $E = \frac{E_0 \nu_F}{a^2 B_0 Gr^{-1/2}}$ are Prandtl number, Weissenberg number, magnetic factor, radiation factor and electric factor, respectively. The appropriate similarity transformation for reducing equations (8) - (11) is as follows:

$$\begin{aligned} &v = \frac{\partial \psi}{\partial y}, \text{ and } w = -\frac{\partial \psi}{\partial x}, \\ &\psi = xF(x,y), \text{and } \theta = \theta(x,y). \end{aligned} \tag{12}$$

Applying the similarity transformation (12) yields:

$$\begin{aligned} &\frac{\rho_F}{\rho_{THNF}} \frac{\mu_{THNF}}{\mu_F} \frac{\partial^3 F}{\partial y^3}\left(1 + We\frac{\partial^2 F}{\partial y^2}\right) - \left(\frac{\partial F}{\partial y}\right)^2 + F\frac{\partial^2 F}{\partial y^2} + \frac{\beta_{THNF}}{\beta_F}\theta\frac{\sin x}{x} \\ &+ \frac{\beta_{THNF}}{\beta_F}\theta\sin x - \frac{\rho_F}{\rho_{THNF}}\frac{\sigma_{THNF}}{\sigma_F} M\left(\frac{\partial F}{\partial y} - E\right) = x\left(\frac{\partial^2 F}{\partial x \partial y} - \frac{\partial F}{\partial x}\frac{\partial^2 F}{\partial y^2}\right), \end{aligned} \tag{13}$$

$$\frac{1}{\Pr}\frac{\left(\rho c_p\right)_F}{\left(\rho c_p\right)_{THNF}}\left(\frac{k_{THNF}}{k_F} + \frac{4}{3}L\right)\frac{\partial^2 \theta}{\partial y^2} + F\frac{\partial \theta}{\partial y} = x\left(\frac{\partial F}{\partial y}\frac{\partial \theta}{\partial x} - \frac{\partial F}{\partial x}\frac{\partial \theta}{\partial y}\right). \tag{14}$$

Subject to:

$$\begin{aligned} &F = \frac{\partial F}{\partial y} = 0,\ \theta = 1 \text{ at } y = 0, \\ &\frac{\partial F}{\partial y} \to 0,\ \theta \to 0 \text{ as } y \to \infty. \end{aligned} \tag{15}$$

As *x* tends towards zero in the vicinity of the critical reference point, the mathematical model reduces to:

$$\frac{\rho_F}{\rho_{THNF}}\frac{\mu_{THNF}}{\mu_F} F'''\left(1 + We\,F''\right) - \left(F'\right)^2 + FF' + \frac{\beta_{THNF}}{\beta_F}\theta - \frac{\rho_F}{\rho_{THNF}}\frac{\sigma_{THNF}}{\sigma_F} M\left(F' - E\right) = 0, \tag{16}$$

$$\frac{1}{\Pr}\frac{\left(\rho c_p\right)_F}{\left(\rho c_p\right)_{THNF}}\left(\frac{k_{THNF}}{k_F} + \frac{4}{3}L\right)\theta'' + F\theta' = 0. \tag{17}$$

Subject to:

$$\begin{aligned} &F = F' = 0,\ \theta = 1 \text{ at } y = 0, \\ &F' \to 0,\ \theta \to 0 \text{ as } y \to \infty. \end{aligned} \tag{18}$$

he following are the mathematical expressions for the Nusselt number Nu and the skin friction C_f (see [39]):

$$Nu = \frac{aq_w}{k_F\left(T_w - T_\infty\right)}, \quad C_f = \frac{\tau_w}{U_\infty^2 \rho_F}. \tag{19}$$

where

$$\begin{aligned} q_w &= -k_{THNF}\left(\frac{\partial T}{\partial \overline{y}}\right)_{\overline{y}=0} + \left(q_r\right)_{\overline{y}=0}, \\ U_\infty^2 &= \frac{Gr\,\nu_F^2}{a^2},\ \tau_w = \mu_{THNF}\left(\frac{\partial \overline{v}}{\partial \overline{y}} + \frac{\Gamma}{\sqrt{2}}\left(\frac{\partial \overline{v}}{\partial \overline{y}}\right)^2\right)_{\overline{y}=0}. \end{aligned} \tag{20}$$

Applying equations (7) and (12) yields the following dimensionless forms of Nu and C_f :

$$\begin{aligned} Gr^{-1/4}Nu &= -\left(\frac{k_{THNF}}{k_F} + \frac{4}{3}L\right)\left(\frac{\partial \theta}{\partial y}\right)_{y=0}, \\ Gr^{1/4}C_f &= \frac{\mu_{THNF}}{\mu_F} x\left(\frac{We}{2}\frac{\partial^2 F}{\partial y^2} + \left(\frac{\partial^2 F}{\partial y^2}\right)^2\right)_{y=0}. \end{aligned} \tag{21}$$

4. Numerical technique and results validation

By synergistically combining Newton's linearization method and the spectral collocation technique, or, as it is termed, the hybrid linearization spectral collocation technique, the governing model of this problem is numerically solved (see [28, 40-42]) [40-42]. Numerical results were calculated using MATLAB with an accuracy of up to 10^{-6} and were subsequently validated by comparing them with existing results, where they showed excellent agreement (see Tables 3 and 4).

Table 3: Comparison of current $Gr^{-1/4}Nu$ results with existing results at Pr = 1, and We = M = L = E = 0.

x in degrees	0	30	60	90	120	150	180
Merkin [43]	0.4214	0.4161	0.4007	0.3745	0.3364	0.2825	0.1945
Molla et al. [44]	0.4241	0.4161	0.4005	0.3740	0.3355	0.2812	0.1917
Current results	0.4213	0.4162	0.4006	0.3741	0.3354	0.2806	0.1926

Table 4: Comparison of current $Gr^{1/4}C_f$ results with existing results at Pr = 1, and We = M = L = E = 0.

x in degrees	0	30	60	90	120	150	180
Merkin [43]	0	0.4151	0.7558	0.9579	0.9756	0.7822	0.3391
Molla et al. [44]	0	0.4145	0.7539	0.9541	0.9696	0.7739	0.3264
Current results	0	0.4153	0.7556	0.9563	0.9714	0.7739	0.3345

5. Graphical representations and discussions

Within this section, graphical predictions of the tri-hybrid nanofluid's' thermal behaviour and flow characteristics are made when it is exposed to the specific factors that are the focus of this investigation, which include thermal radiation, an electric field, and a magnetic field. Additionally, an assessment of the extent to which nanosolid shape, nanosolid volume fraction, and the Weissenberg number influence these thermal and flow characteristics is provided. The cumulative nanosolid volume fractions are equal to 1, 3, and 5%. Additionally, Table 5. shows the volume fractions of nanosolids employed to formulate the tri-hybrid nanoliquid Al_2O_3-TiO_2-Cu/H_2O.

Table 5: Volume fractions of nanosolids employed to formulate Al_2O_3-TiO_2-Cu/H_2O.

volume fraction of Al_2O_3 nanosolids %	volume fraction of TiO_2 nanosolids %	volume fraction of Cu nanosolids %	Cumulative volume fraction %
0. 4	0. 4	0. 2	1
1.2	1.2	0.6	3
2	2	1	5

Fig 2 illustrates the relationship between the Nusselt number and the Weissenberg number. It is clear that as the Weissenberg number rises, there is a distinct decrease in heat transfer improvement for the tri-hybrid nanofluid. The impact of the Weissenberg number on diminished heat transfer is particularly significant in the case of the tri-hybrid nanofluid. This occurrence can be attributed to the rise in the Weissenberg number, which hinders fluid deformation, elevates the fluid's viscosity, and restricts the extent of energy transport. Fig 3 presents the trends observed in the Nusselt number when subjected to escalating thermal radiation while holding all other examined factors constant. Notably, an evident upward trajectory is witnessed in the Nusselt number as thermal radiation intensifies, indicating a proportional augmentation in the rate of energy transfer. This behaviour aligns with expectations, as an increase in the radiation factor signifies more energy emitted into the fluid, consequently leading to an amplified heat transfer rate. Furthermore, it is noteworthy that the impact of thermal radiation on the hybrid and tri-hybrid nanofluids surpasses its influence on the conventional fluid, suggesting a heightened sensitivity of the former to changes in radiation levels. Fig 4 exhibits the variations in the Nusselt number imposed by the escalating magnetic factor while keeping the other examined factors constant. Evidently, as the magnetic parameter increases, there is a conspicuous decay in the Nusselt number. This behaviour aligns with the expected trend, as the augmentation of the magnetic field strength instigates the generation of the Lorentz force, which in turn hampers fluid velocity, consequently impeding the range of heat transmission. Fig 5 depicts the impact of augmenting the volume fraction factor on the Nusselt number while keeping all other examined parameters constant. Evidently, an increase in the volume fraction factor corresponds to a notable elevation in the Nusselt number. This phenomenon can be attributed to the enhanced thermal conductivity of the host fluid, facilitated by the higher volume fraction factor. Furthermore, even a slight increment in the volume fraction factor intensifies the buoyancy forces, thereby augmenting the rate of energy transfer.

In Fig 6, a portrayal of the influence occurring by enhancing the electrical factor on the Nusselt number is presented. A higher Nusselt number is observed with a higher electrical factor. Enhanced fluid motion, altered boundary layer profiles, and additional heat generation are responsible for the increase in the Nusselt number when the electric factor increases. Fig 7 provides a visual depiction of the interplay between the Weissenberg number and skin friction. The coefficient of skin friction experiences a discernible decline as the Weissenberg number ascends. An enhancement in the relaxation time corresponds with a surge in the Weissenberg number, subsequently resulting in diminished drag forces. Skin friction is clearly shown as an increasing function of the radiation factor in Fig 8. The increased skin contacts between the nanofluid and the cylinder in the presence of enhanced thermal radiation can be understood as a result of intensified heat absorption and enhanced convective heat transfer. These factors work together to promote a more intimate interaction between the nanofluid and the cylinder surface, leading to increased skin friction.

Fig 9 visually elucidates the relationship between the augmentation of magnetic field intensity and its consequential impact on skin friction. As the magnetic field strength intensifies, it exerts a pronounced influence on the charged particles embedded within the nanofluid. Emanating as the Lorentz force, this magnetic impetus manifests in a direction perpendicular to both the magnetic field and the fluid's velocity, ushering in a reduction of the fluid velocity proximate to the cylinder surface. Consequently, this change engenders a reduction in the exertion of frictional forces.

Fig 10 demonstrates that the behaviour of skin friction exhibits an increasing trend in response to the augmentation of the volume fraction factor. There is a noticeable amplifying of the resistance that the fluid flow over the surface encounters as the volume fraction factor rises. Consequently, this elevated resistance leads to a discernible rise in drag forces and a consequential escalation in skin friction.

Fig 11 depicts an elucidation of the interplay between the augmentation of the electrical factor and its consequential impact on the behaviour of skin friction. It is observed that skin friction behaves as an increasing function of the electric field factor. The

increased electrical factor raises fluid temperature at the cylinder surface, changing fluid viscosity and density and influencing boundary layer characteristics. These alterations can alter flow and increase skin friction.

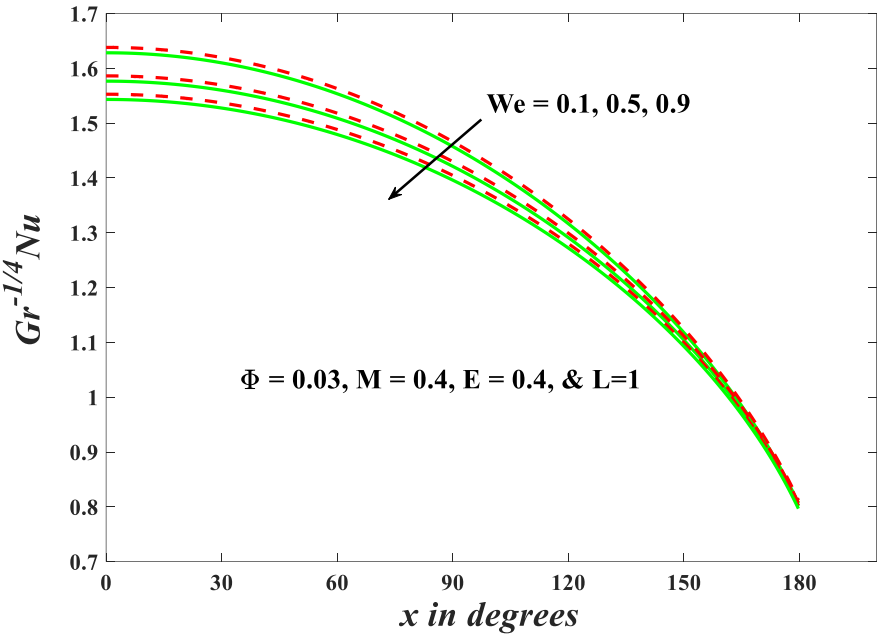

Fig 2: Impression of *We* on the Nusselt number
Green curve: Al_2O_3(spheres), TiO_2(spheres), Cu(spheres)
Red dashed curve: Al_2O_3(hexahedrons), TiO_2(tetrahedrons), Cu(laminas)

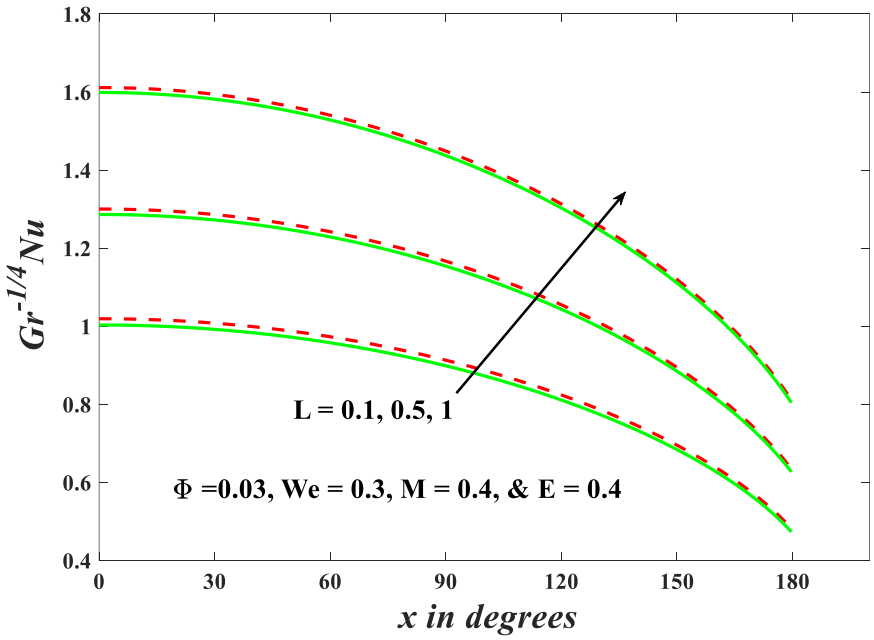

Fig 3: Impression of *L* on the Nusselt number
Green curve: Al_2O_3(spheres), TiO_2(spheres), Cu(spheres)
Red dashed curve: Al_2O_3(hexahedrons), TiO_2(tetrahedrons), Cu(laminas)

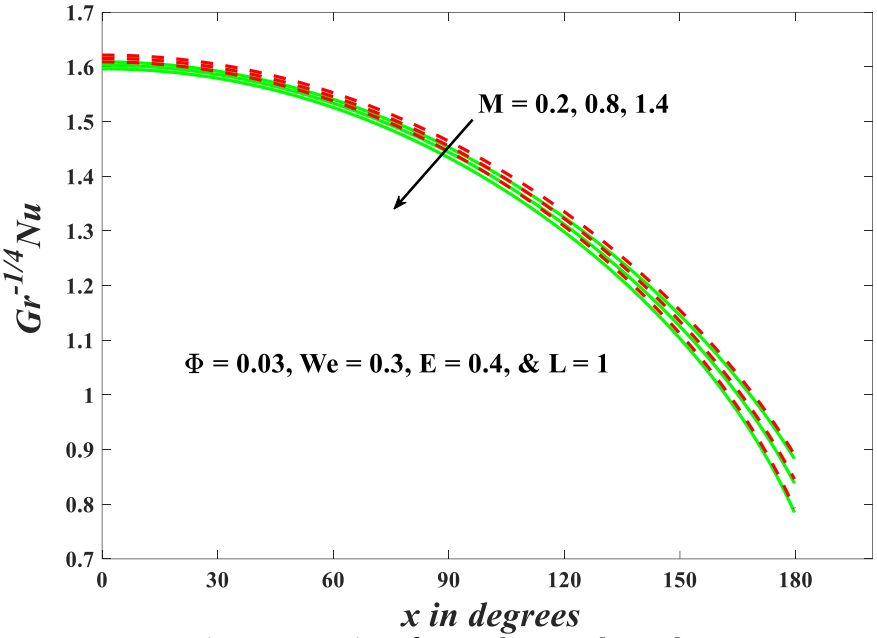

Fig 4: Impression of *M* on the Nusselt number
Green curve: Al_2O_3(spheres), TiO_2(spheres), Cu(spheres)
Red dashed curve: Al_2O_3(hexahedrons), TiO_2(tetrahedrons), Cu(laminas)

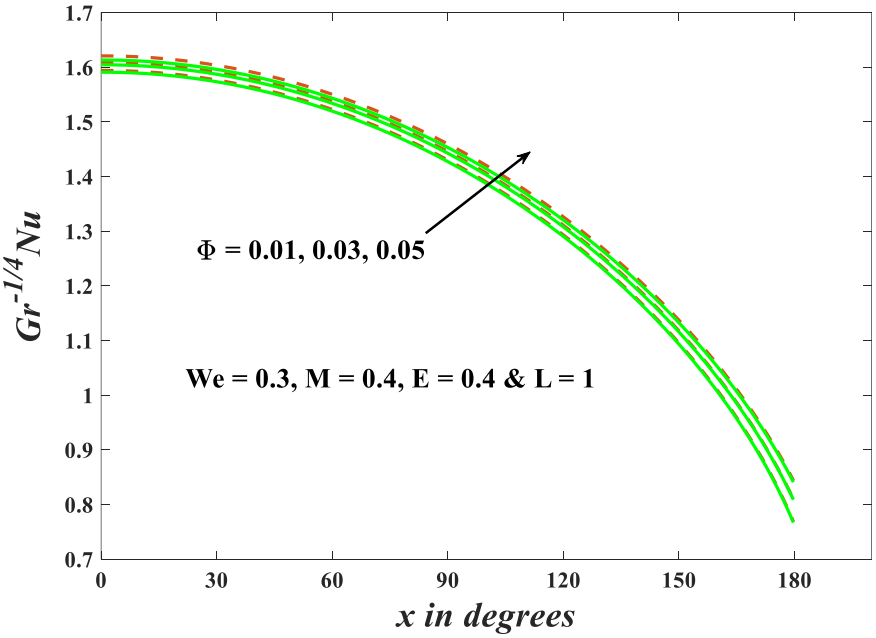

Fig 5: Impression of Φ on the Nusselt number.
Green curve: Al_2O_3(spheres), TiO_2(spheres), Cu(spheres)
Red dashed curve: Al_2O_3(hexahedrons), TiO_2(tetrahedrons), Cu(laminas)

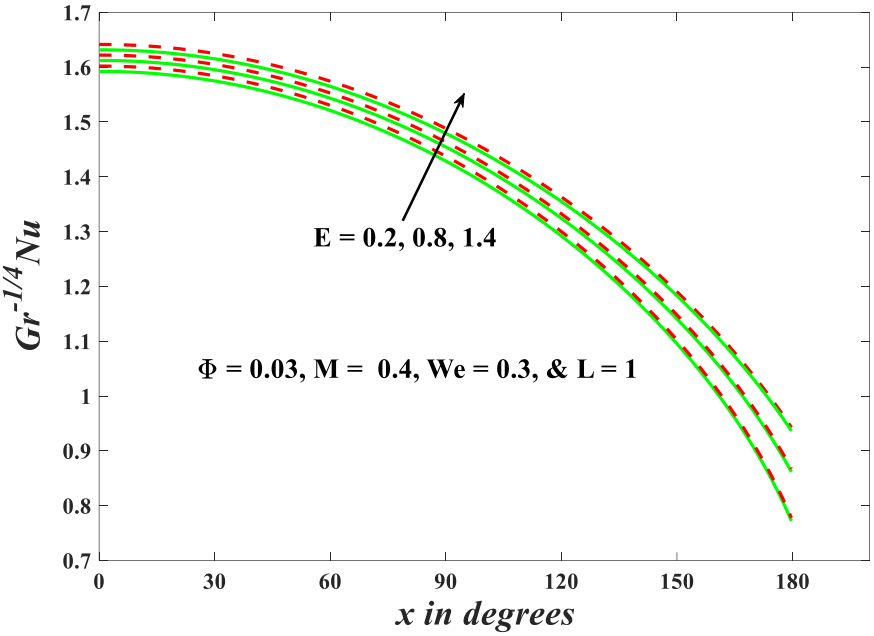

Fig 6: Impression of *E* on the Nusselt number
Green curve: Al_2O_3(spheres), TiO_2(spheres), Cu(spheres)
Red dashed curve: Al_2O_3(hexahedrons), TiO_2(tetrahedrons), Cu(laminas)

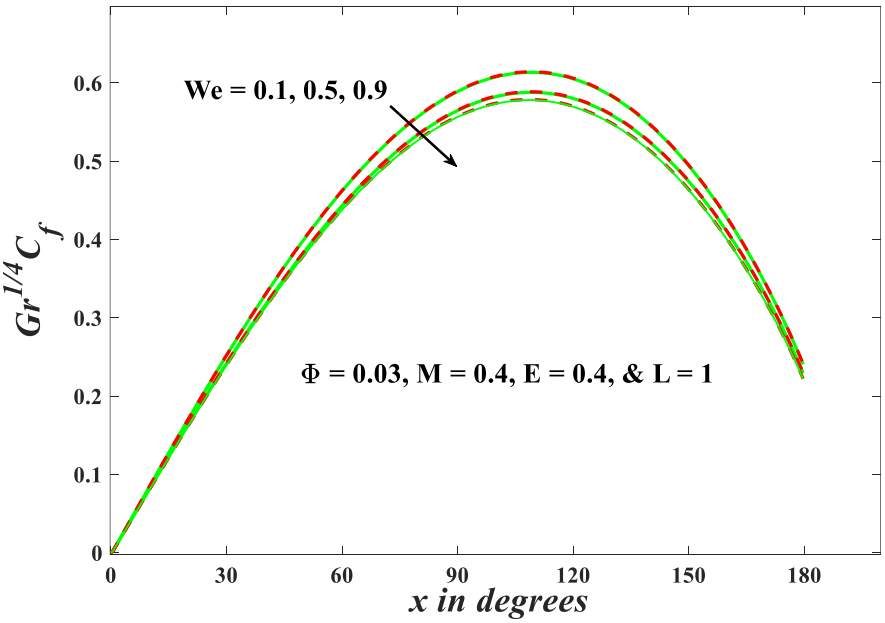

Fig 7: Impression of *We* on the skin friction
Green curve: Al_2O_3(spheres), TiO_2(spheres), Cu(spheres)
Red dashed curve: Al_2O_3(hexahedrons), TiO_2(tetrahedrons), Cu(laminas)

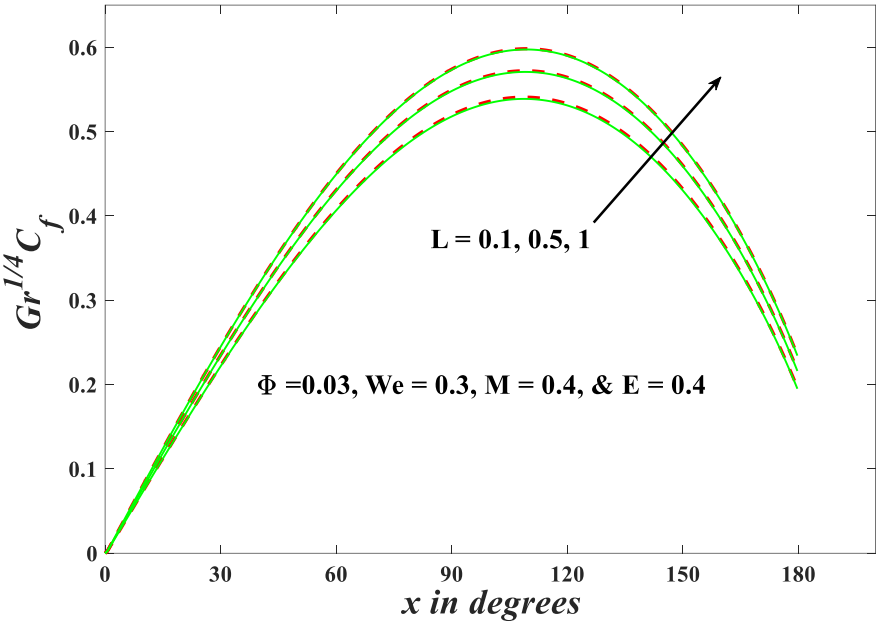

Fig 8: Impression of *L* on the skin friction

Green curve: Al_2O_3(spheres), TiO_2(spheres), Cu(spheres)
Red dashed curve: Al_2O_3(hexahedrons), TiO_2(tetrahedrons), Cu(laminas)

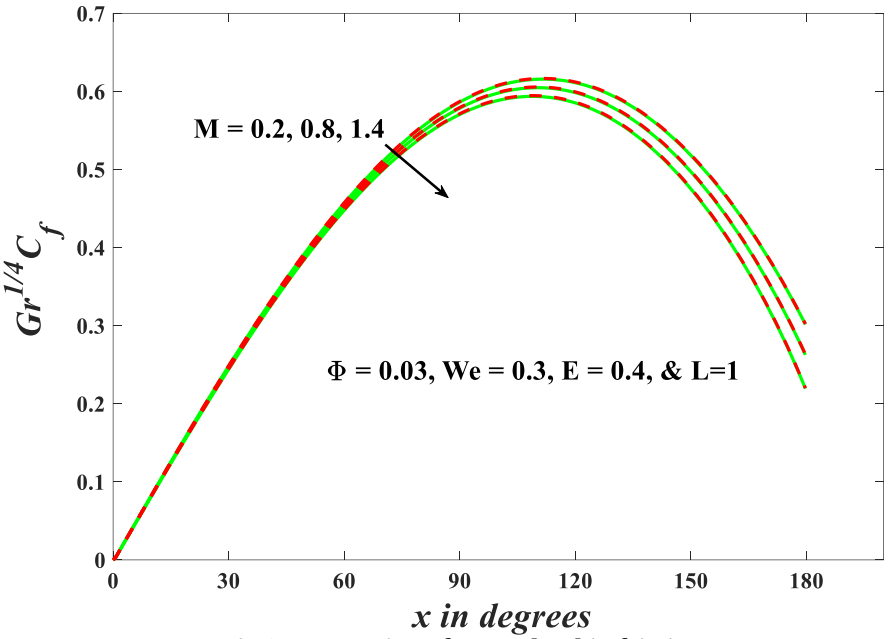

Fig 9: Impression of *M* on the skin friction

Green curve: Al_2O_3(spheres), TiO_2(spheres), Cu(spheres)
Red dashed curve: Al_2O_3(hexahedrons), TiO_2(tetrahedrons), Cu(laminas)

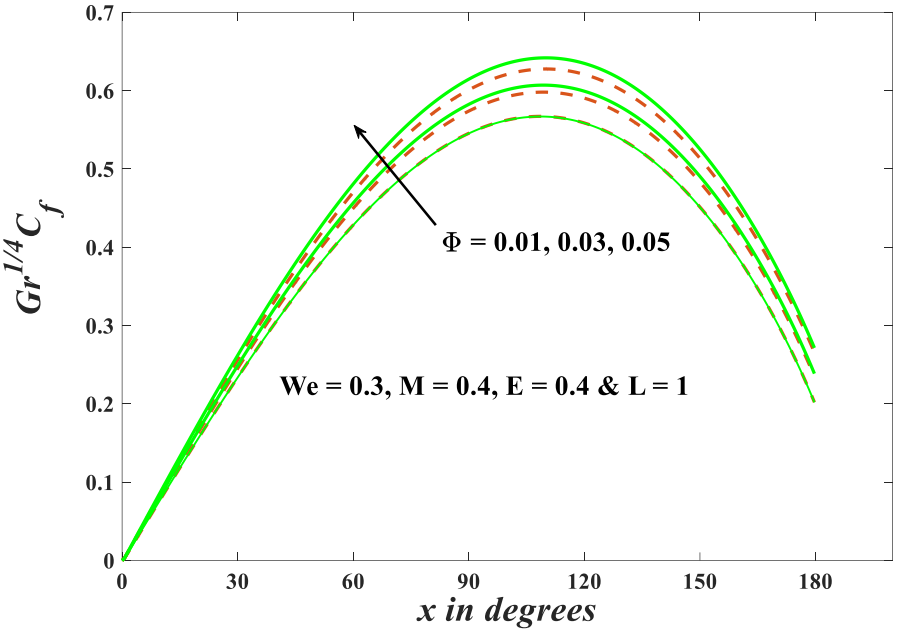

Fig 10: Impression of Φ on the skin friction
Green curve: Al_2O_3(spheres), TiO_2(spheres), Cu(spheres)
Red dashed curve: Al_2O_3(hexahedrons), TiO_2(tetrahedrons), Cu(laminas)

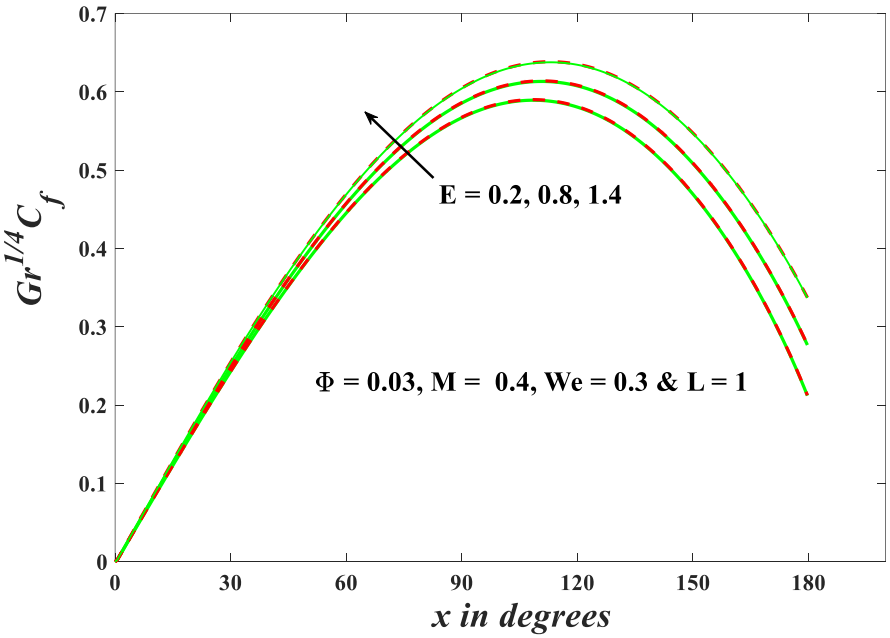

Fig 11: Impression of *E* on the skin friction
Green curve: Al_2O_3(spheres), TiO_2(spheres), Cu(spheres)
Red dashed curve: Al_2O_3(hexahedrons), TiO_2(tetrahedrons), Cu(laminas)

Fig 12 offers a visual portrayal of the trends in velocity profiles arising from the progressive amplification of the Weissenberg number. The observed decrease in fluid velocity with an increase in the Weissenberg number can be attributed to the enhanced influence of viscoelastic effects on the fluid flow. As the Weissenberg number increases, it signifies a higher dominance of the fluid's elasticity over its viscosity. This increased elasticity leads to the formation of more pronounced viscoelastic stresses within the nanofluid, which in turn resist and impede fluid motion.

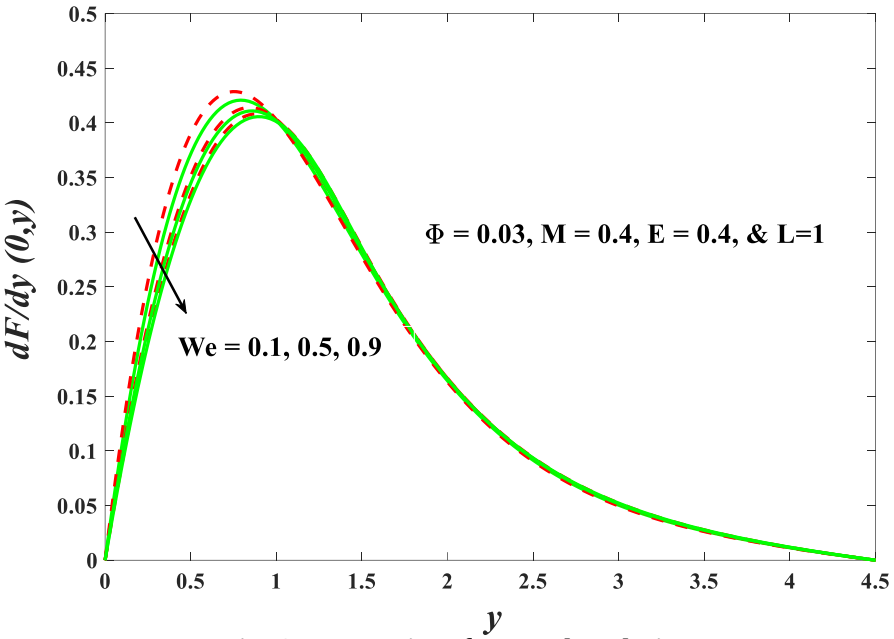

Fig 12: Impression of *We* on the velocity
Green curve: Al_2O_3(spheres), TiO_2(spheres), Cu(spheres)
Red dashed curve: Al_2O_3(hexahedrons), TiO_2(tetrahedrons), Cu(laminas)

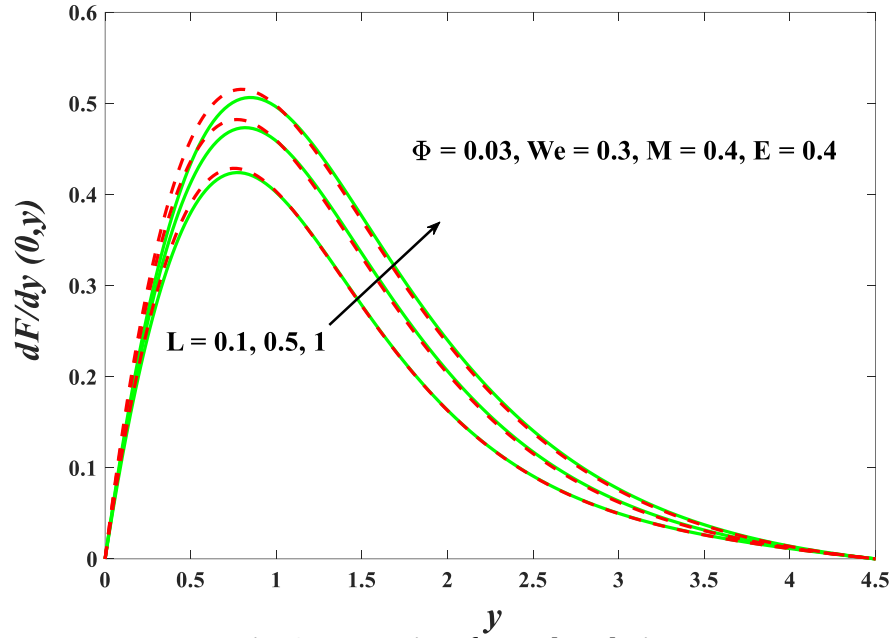

Fig 13: Impression of *L* on the velocity
Green curve: Al_2O_3(spheres), TiO_2(spheres), Cu(spheres)
Red dashed curve: Al_2O_3(hexahedrons), TiO_2(tetrahedrons), Cu(laminas)

The tri-hybrid Williamson nanoliquid velocity distribution affected by the radiation factor is shown in Fig 13. When radiation intensity increases, the tri-hybrid Williamson nanoliquid and the cylinder surface receive more thermal energy through radiation. This additional energy leads to an increase in the temperature of the tri-hybrid Williamson nanoliquid near the surface. As the temperature rises, the fluid's density decreases, creating a buoyancy force that drives fluid motion. Consequently, the fluid velocity increases as a result of enhanced convective heat transfer.

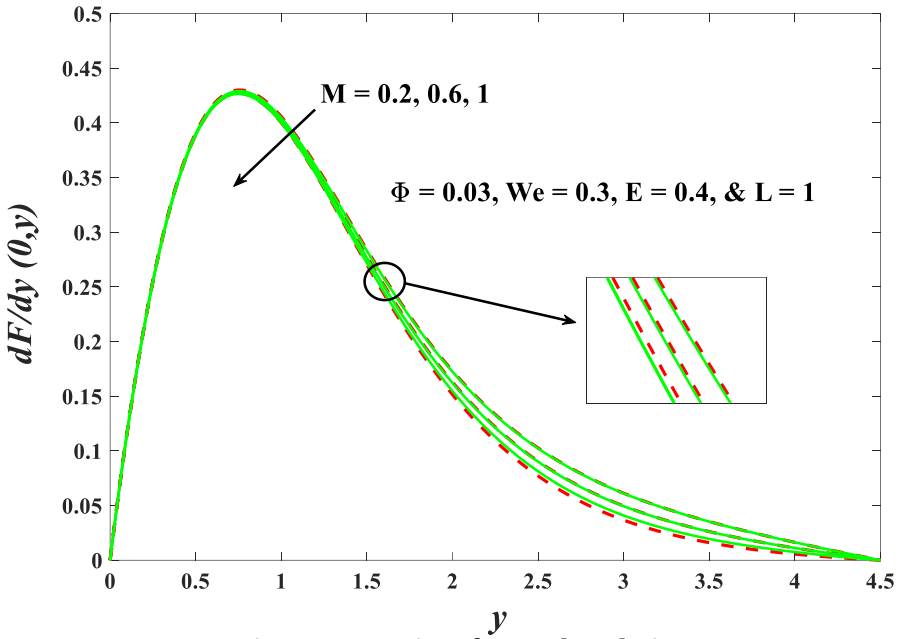

Fig 14: Impression of M on the velocity
Green curve: Al_2O_3(spheres), TiO_2(spheres), Cu(spheres)
Red dashed curve: Al_2O_3(hexahedrons), TiO_2(tetrahedrons), Cu(laminas)

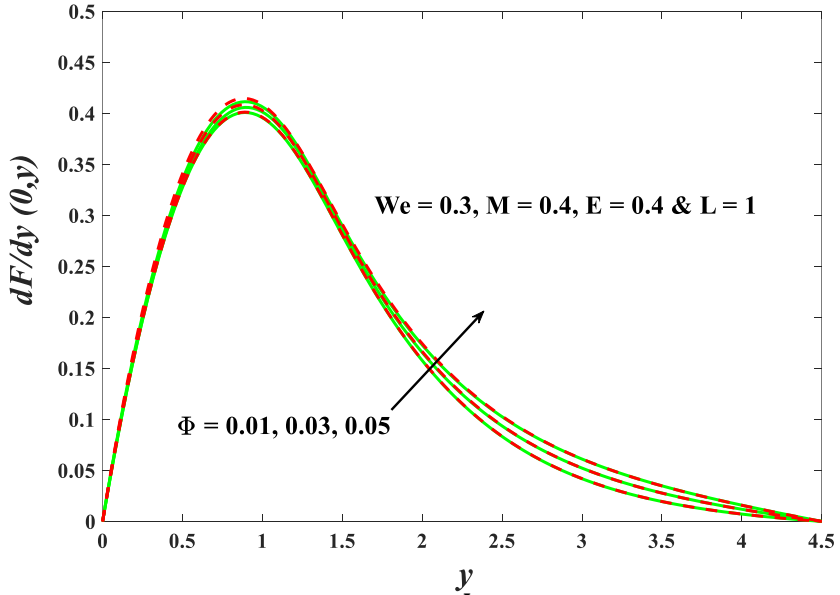

Fig 15: Impression of Φ on the velocity
Green curve: Al_2O_3(spheres), TiO_2(spheres), Cu(spheres)
Red dashed curve: Al_2O_3(hexahedrons), TiO_2(tetrahedrons), Cu(laminas)

Fig 14 elucidates the implications of augmenting magnetic parameter values on the velocity of tri-hybrid Williamson nanoliquid. When the magnetic factor increases, the formation of Lorentz forces is stimulated. As the magnetic field becomes stronger, the Lorentz force becomes more significant, exerting a greater influence on the fluid motion. Consequently, the fluid velocity tends to decrease as the magnetic field strength increases.

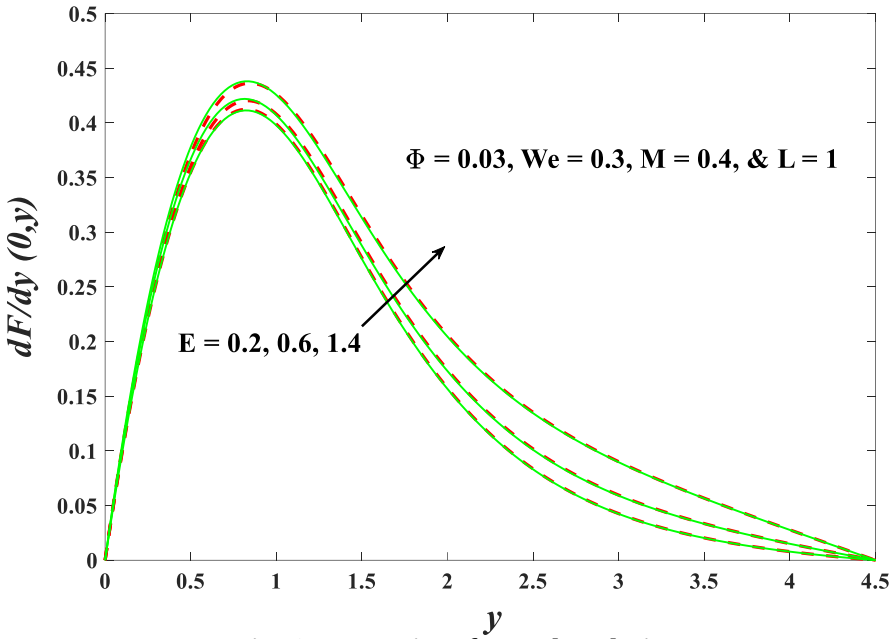

Fig 16: Impression of *E* on the velocity
Green curve: Al_2O_3(spheres), TiO_2(spheres), Cu(spheres)
Red dashed curve: Al_2O_3(hexahedrons), TiO_2(tetrahedrons), Cu(laminas)

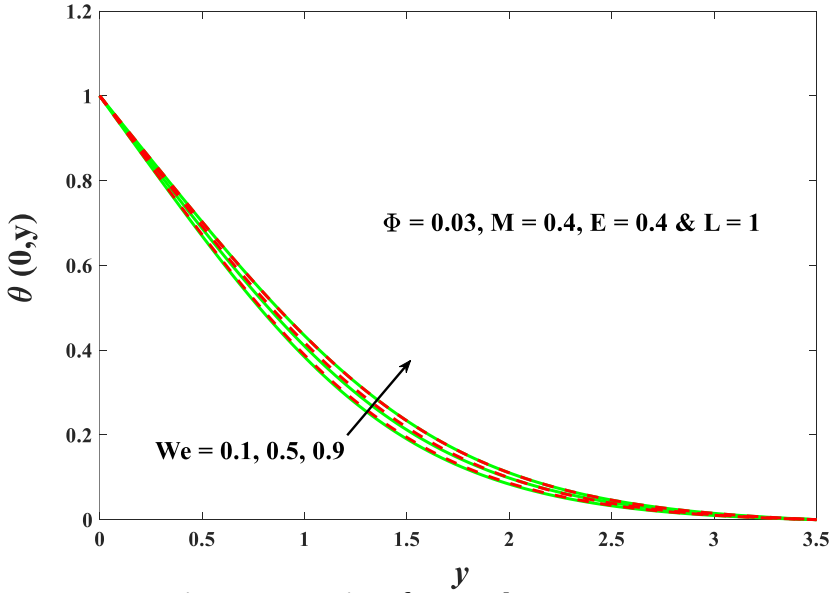

Fig 17: Impression of *We* on the temperature
Green curve: Al_2O_3(spheres), TiO_2(spheres), Cu(spheres)
Red dashed curve: Al_2O_3(hexahedrons), TiO_2(tetrahedrons), Cu(laminas)

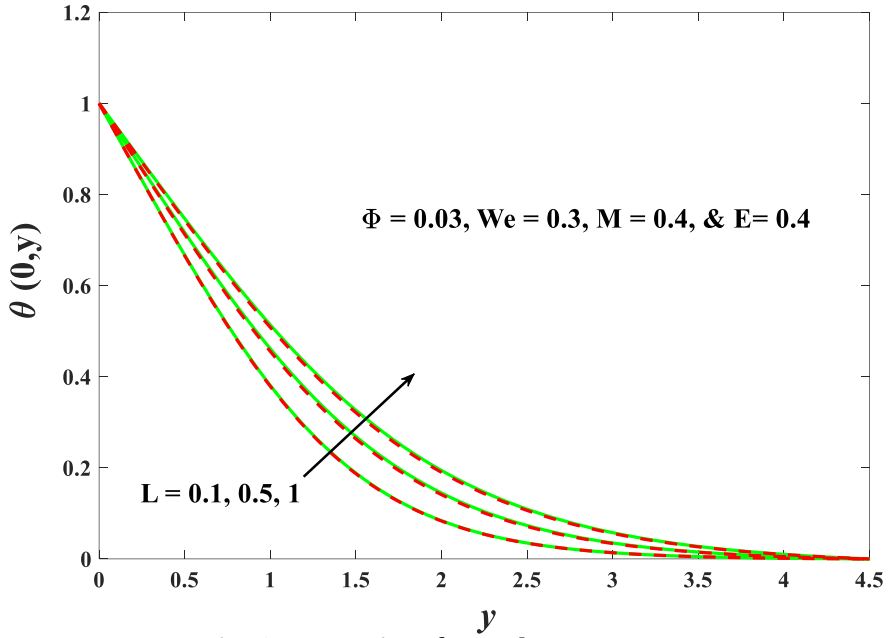

Fig 18: Impression of L on the temperature

Green curve: Al_2O_3(spheres), TiO_2(spheres), Cu(spheres)

Red dashed curve: Al_2O_3(hexahedrons), TiO_2(tetrahedrons), Cu(laminas)

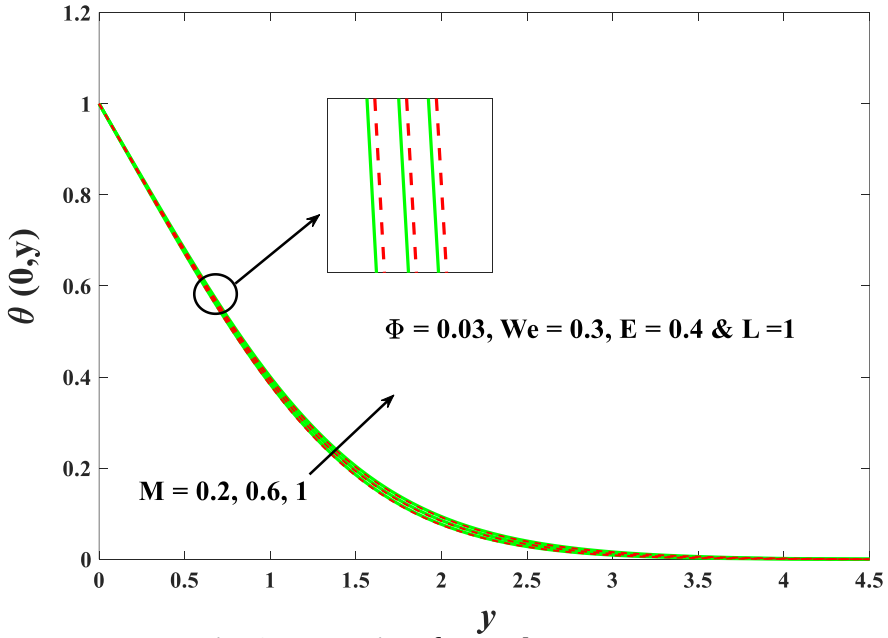

Fig 19: Impression of *M* on the temperature

Green curve: Al_2O_3(spheres), TiO_2(spheres), Cu(spheres)

Red dashed curve: Al_2O_3(hexahedrons), TiO_2(tetrahedrons), Cu(laminas)

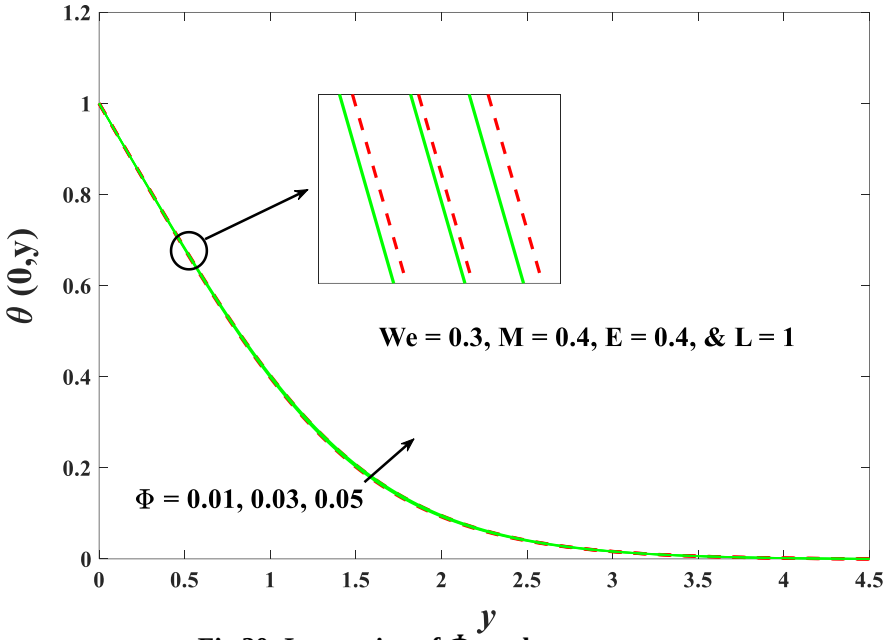

Fig 20: Impression of Φ on the temperature
Green curve: Al_2O_3(spheres), TiO_2(spheres), Cu(spheres)
Red dashed curve: Al_2O_3(hexahedrons), TiO_2(tetrahedrons), Cu(laminas)

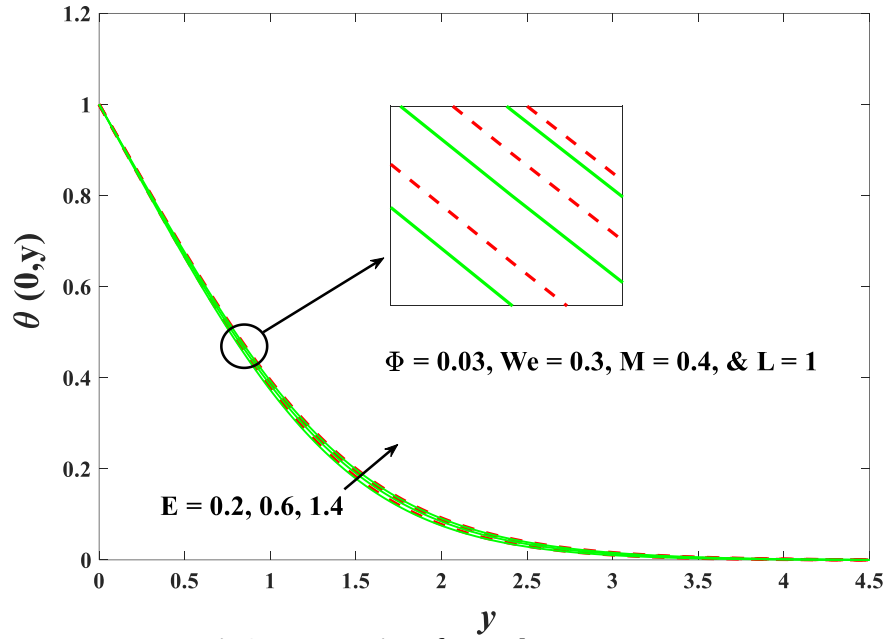

Fig 21: Impression of *E* on the temperature
Green curve: Al_2O_3(spheres), TiO_2(spheres), Cu(spheres)
Red dashed curve: Al_2O_3(hexahedrons), TiO_2(tetrahedrons), Cu(laminas)

The graphical representation in Fig 15 reveals the positive effect of the volume fraction factor on the velocity of the original fluid. The augmentation of the volume fraction factor exhibits a discernible amelioration in velocity profiles, primarily attributed to the concurrent escalation in the thermal conductivity of the original fluid. Fig 16 provides a visual depiction of the interplay between the electrical factor and velocity of tri-hybrid nanoliquid. It is observed that there is an increase in the tri-hybrid nanoliquid velocity as the electrical factor increases. When an electric current is applied, the electric field interacts with the charged particles, causing them to move. This movement creates a net tri-hybrid Williamson nanoliquid flow in the direction opposite to the movement of the charged particles, resulting in an increase in fluid velocity. Fig 17 elucidates the transformative variations in temperature profiles induced by the progressive escalation of Weissenberg number values. The fluid temperature exhibits a pronounced elevation commensurate with the increasing Weissenberg number, owing to the simultaneous escalating relaxation time. Fig 18 unveils the affirmative implications of elevating the radiation factor on the temperature of tri-hybrid Williamson nanoliquid. As the radiation factor increases, the contribution of radiative heat transfer becomes more significant, leading to additional heat input into the tri-hybrid Williamson nanoliquid, resulting in a rise in its temperature. Fig 19 reveals the influence of augmenting the magnetic parameter on the temperature of the tri-hybrid Williamson nanoliquid. The augmentation of the magnetic parameter is unequivocally accompanied by a discernible elevation in the liquid temperature. This phenomenon arises from the induction of Lorentz forces, which engender a distinctive form of friction exerting a profound impact on fluid flow dynamics. Consequently, the temperature of tri-hybrid Williamson nanoliquid exhibits a notable ascent as an outcome of the supplementary heat energy generated by these frictional forces. Fig 20 unveils a positive correlation between the original fluid temperature and the volume fraction factor of the tri-hybrid Williamson nanoliquid. Augmenting the volume fraction factor yields an enhancement in the thermal conductivity of the host fluid, thereby fostering an accelerated rate of energy transfer. This heightened energy transfer manifests as an upsurge in temperature. In Fig 21, the relationship between increasing the electrical factor and its effect on the temperature behaviour of the tri-hybrid Williamson nanoliquid is shown. It is clear that there is a direct proportionality between the electrical factor and the tri-hybrid Williamson nanoliquid temperature. The electric current involves the transfer of charged particles, typically electrons, through the fluid. As these charged particles move, they collide with atoms or molecules in the fluid. These collisions transfer energy to the atoms, resulting in an increase in their kinetic energy and the overall thermal energy of the fluid. This increased thermal energy leads to a rise in fluid temperature.

6. Conclusion

A numerical analysis of EMHD tri-hybrid Williamson liquid flow around a cylinder was carried out, with particular emphasis on the effect of radiation and nanosolids shape parameters, which, to the best of the authors' knowledge, have not been addressed in the literature. Listed below are the main findings from the present investigation:

- The Nusselt number shows a positive correlation with thermal radiation, indicating increased energy transfer. Conversely, it decreases as the magnetic parameter increases. Moreover, the Nusselt number rises with a higher volume fraction of nanoparticles.
- Higher volume fractions or radiation factors are associated with increased skin friction, while increasing Weissenberg numbers or higher magnetic field strengths have the opposite effect, reducing skin friction.
- Fluid velocity decreases with a higher Weissenberg number and tends to decrease with increasing magnetic field strength. However, increasing the volume fraction factor improves velocity profiles.
- The tri-hybrid Williamson nanoliquid temperature experiences a notable increase with a higher Weissenberg number, thermal radiation, and magnetic parameter.
- With increasing volume fraction, using Al_2O_3(hexahedron) - TiO_2(tetrahedron) - Cu(lamina) / H_2O raises the Nusselt number by 0.02 - 5% while decreasing skin friction by 1.3 - 9% compared with using Al_2O_3(sphere)-TiO_2(sphere)-Cu(sphere)/H_2O.

Numerous future studies can be explored in light of the results of this work, using different mathematical models, like the Casson model. It can further explore the same topic in future work by investigating the impact of viscous dissipation, joule heating, etc.

Funding statement
The authors extend their appreciation to Prince Sattam bin Abdulaziz University for funding this research work through the project number (PSAU/2023/01/25361).

Nomenclature

a	Cylinder's radius
B_0	Strength of the magnetic field
C_f.	Skin friction factor
E	Electrical factor
Gr	Grashof number

g	Gravity vector
k	Thermal conductivity
L	Radiation factor
M	Magnetic factor
m	Shape factor
Nu	Nusselt Number
Pr	Prandtl number
T_∞	Ambient temperature
T_w	Wall temperature
v	Component of velocity
v_F	Kinematic viscosity
w	Component of velocity
We	Weissenberg number
x,y	Dimensional variables along velocity component v, w
Φ	Volume fraction factor
σ	Electrical conductivity
ψ	Stream function
β	Thermal expansion factor
ρc_p	Heat capacity
μ	Dynamic viscosity
ρ	Density
θ	Temperature
Subscript	
F	Host liquid
NF	Mono nanoliquid
HNF	Hybrid nanoliquid
$THNF$	Ternary hybrid nanoliquid

References

[1] R. V. Williamson, The flow of pseudoplastic materials, *Industrial & Engineering Chemistry*, Vol. 21, No. 11, pp. 1108-1111, 1929.

[2] S. Bilal, K. U. Rehman, M. Malik, Numerical investigation of thermally stratified Williamson fluid flow over a cylindrical surface via Keller box method, *Results in physics*, Vol. 7, pp. 690-696, 2017.

[3] W. Ibrahim, M. Negera, Viscous dissipation effect on mixed convective heat transfer of MHD flow of Williamson nanofluid over a stretching cylinder in the presence of variable thermal conductivity and chemical reaction, *Heat Transfer*, Vol. 50, No. 3, pp. 2427-2453, 2021.

[4] F. A. Alwawi, F. M. Al Faqih, M. Z. Swalmeh, M. A. H. Ibrahim, Combined convective energy transmission performance of Williamson hybrid nanofluid over a cylindrical shape with magnetic and radiation impressions, *Mathematics*, Vol. 10, No. 17, pp. 3191, 2022.

[5] K. B. S. Latha, M. G. Reddy, D. Tripathi, O. A. Bég, S. Kuharat, H. Ahmad, D. U. Ozsahin, S. Askar, Computation of stagnation coating flow of electro-conductive ternary Williamson hybrid GO-AU-Co 3 O 4/EO nanofluid with a Cattaneo–Christov heat flux model and magnetic induction, *Scientific Reports*, Vol. 13, No. 1, pp. 10972, 2023.

[6] M. Z. Swalmeh, F. A. Alwawi, M. S. Kausar, M. A. H. Ibrahim, A. S. Hamarsheh, I. M. Sulaiman, A. M. Awwal, N. Pakkaranang, B. Panyanak, Numerical simulation on energy transfer enhancement of a Williamson ferrofluid subjected to thermal radiation and a magnetic field using hybrid ultrafine particles, *Scientific Reports*, Vol. 13, No. 1, pp. 3176, 2023.

[7] O. A. S. Alzu'bi, F. A. Alwawi, M. Z. Swalmeh, I. M. Sulaiman, A. S. Hamarsheh, M. A. H. Ibrahim, Energy transfer through a magnetized williamson hybrid nanofluid flowing around a spherical surface: Numerical simulation, *Mathematics*, Vol. 10, No. 20, pp. 3823, 2022.

[8] H. Adun, D. Kavaz, M. Dagbasi, Review of ternary hybrid nanofluid: Synthesis, stability, thermophysical properties, heat transfer applications, and environmental effects, *Journal of Cleaner Production*, Vol. 328, pp. 129525, 2021.

[9] R. Rekha Sahoo, Effect of various shape and nanoparticle concentration based ternary hybrid nanofluid coolant on the thermal performance for automotive radiator, *Heat and Mass Transfer*, Vol. 57, No. 5, pp. 873-887, 2021.

[10] V. Kumar, R. R. Sahoo, Experimental and numerical study on cooling system waste heat recovery for engine air preheating by ternary hybrid nanofluid, *Journal of Enhanced Heat Transfer*, Vol. 28, No. 4, 2021.

[11] A. Dezfulizadeh, A. Aghaei, A. Hassani Joshaghani, M. M. Najafizadeh, Exergy efficiency of a novel heat exchanger under MHD effects filled with water-based Cu–SiO2-MWCNT ternary hybrid nanofluid based on empirical data, *Journal of Thermal Analysis and Calorimetry,* Vol. 147, No. 7, pp. 4781-4804, 2022.

[12] Z. Mahmood, S. E. Alhazmi, U. Khan, M. Z. Bani-Fwaz, A. M. Galal, Unsteady MHD stagnation point flow of ternary hybrid nanofluid over a spinning sphere with Joule heating, *International Journal of Modern Physics B,* Vol. 36, No. 32, pp. 2250230, 2022.

[13] F. A. Alwawi, M. Z. Swalmeh, A. S. Hamarsheh, Computational simulation and parametric analysis of the effectiveness of ternary nano-composites in improving magneto-micropolar liquid heat transport performance, *Symmetry,* Vol. 15, No. 2, pp. 429, 2023.

[14] M. Mumtaz, S. Islam, H. Ullah, Z. Shah, Chemically reactive MHD convective flow and heat transfer performance of ternary hybrid nanofluid past a curved stretching sheet, *Journal of Molecular Liquids,* Vol. 390, pp. 123179, 2023.

[15] K.-L. Hsiao, Combined electrical MHD heat transfer thermal extrusion system using Maxwell fluid with radiative and viscous dissipation effects, *Applied Thermal Engineering,* Vol. 112, pp. 1281-1288, 2017.

[16] O. U. Mehmood, M. M. Maskeen, A. Zeeshan, Electromagnetohydrodynamic transport of Al2O3 nanoparticles in ethylene glycol over a convectively heated stretching cylinder, *Advances in Mechanical Engineering,* Vol. 9, No. 11, pp. 1687814017735282, 2017.

[17] S. Jakeer, S. Reddy, A. Rashad, M. L. Rupa, C. Manjula, Nonlinear analysis of Darcy-Forchheimer flow in EMHD ternary hybrid nanofluid (Cu-CNT-Ti/water) with radiation effect, *Forces in Mechanics,* Vol. 10, pp. 100177, 2023.

[18] S. Kumar, S. K. Prasad, J. Banerjee, Analysis of flow and thermal field in nanofluid using a single phase thermal dispersion model, *Applied Mathematical Modelling,* Vol. 34, No. 3, pp. 573-592, 2010.

[19] M. Sheikholeslami, S. Shehzad, Numerical analysis of Fe3O4–H2O nanofluid flow in permeable media under the effect of external magnetic source, *International Journal of Heat and Mass Transfer,* Vol. 118, pp. 182-192, 2018.

[20] A. H. Ghobadi, M. G. Hassankolaei, A numerical approach for MHD Al2O3–TiO2/H2O hybrid nanofluids over a stretching cylinder under the impact of shape factor, *Heat Transfer—Asian Research,* Vol. 48, No. 8, pp. 4262-4282, 2019.

[21] M. Shanmugapriya, R. Sundareswaran, P. S. Kumar, G. Rangasamy, Impact of nanoparticle shape in enhancing heat transfer of magnetized ternary hybrid nanofluid, *Sustainable Energy Technologies and Assessments,* Vol. 53, pp. 102700, 2022.

[22] R. R. Sahoo, Heat transfer and second law characteristics of radiator with dissimilar shape nanoparticle-based ternary hybrid nanofluid, *Journal of Thermal Analysis and Calorimetry,* Vol. 146, No. 2, pp. 827-839, 2021.

[23] R. R. Sahoo, Thermo-hydraulic characteristics of radiator with various shape nanoparticle-based ternary hybrid nanofluid, *Powder technology,* Vol. 370, pp. 19-28, 2020.

[24] M. Sheikholeslami, T. Hayat, A. Alsaedi, MHD free convection of Al2O3–water nanofluid considering thermal radiation: a numerical study, *International Journal of Heat and Mass Transfer,* Vol. 96, pp. 513-524, 2016.

[25] S. EL-Kabeir, A. Rashad, W. Khan, Z. M. Abdelrahman, Micropolar ferrofluid flow via natural convective about a radiative isoflux sphere, *Advances in Mechanical Engineering,* Vol. 13, No. 2, pp. 1687814021994392, 2021.

[26] S. A. Lone, S. Anwar, Z. Raizah, P. Kumam, T. Seangwattana, A. Saeed, Analysis of the time-dependent magnetohydrodynamic Newtonian fluid flow over a rotating sphere with thermal radiation and chemical reaction, *Heliyon,* Vol. 9, No. 7, 2023.

[27] M. Z. Swalmeh, F. Shatat, F. A. Alwawi, M. A. H. Ibrahim, I. M. Sulaiman, N. Yaseen, M. F. Naser, Effectiveness of radiation on magneto-combined convective boundary layer flow in polar nanofluid around a spherical shape, *Fractal and Fractional,* Vol. 6, No. 7, pp. 383, 2022.

[28] E. A. El-Sayed, F. A. Alwawi, F. Aljuaydi, M. Z. Swalmeh, Computational insights into shape effects and heat transport enhancement in MHD-free convection of polar ternary hybrid nanofluid around a radiant sphere, *Scientific Reports,* Vol. 14, No. 1, pp. 1225, 2024.

[29] R. HAMILTO, Thermal conductivity of heterogeneous two-component systems, *I&EC Fundamentals,* Vol. 1, pp. 182-187, 1962.

[30] I. Zahmatkesh, M. Sheremet, L. Yang, S. Z. Heris, M. Sharifpur, J. P. Meyer, M. Ghalambaz, S. Wongwises, D. Jing, O. Mahian, Effect of nanoparticle shape on the performance of thermal systems utilizing nanofluids: A critical review, *Journal of Molecular Liquids,* Vol. 321, pp. 114430, 2021.

[31] Y. Lin, B. Li, L. Zheng, G. Chen, Particle shape and radiation effects on Marangoni boundary layer flow and heat transfer of copper-water nanofluid driven by an exponential temperature, *Powder Technology,* Vol. 301, pp. 379-386, 2016.

[32] S. U. Jan, U. Khan, M. Abd El-Rahman, S. Islam, A. M. Hassan, A. Ullah, Effect of variable thermal conductivity of ternary hybrid nanofluids over a stretching sheet with convective boundary conditions and magnetic field, *Results in Engineering,* Vol. 20, pp. 101531, 2023.

[33] T. Hayat, B. Ahmed, F. Abbasi, A. Alsaedi, Hydromagnetic peristalsis of water based nanofluids with temperature dependent viscosity: a comparative study, *Journal of Molecular Liquids,* Vol. 234, pp. 324-329, 2017.

[34] H. F. Oztop, E. Abu-Nada, Numerical study of natural convection in partially heated rectangular enclosures filled with nanofluids, *International journal of heat and fluid flow*, Vol. 29, No. 5, pp. 1326-1336, 2008.

[35] M. Sheikholeslami, M. Gorji-Bandpy, D. Ganji, Numerical investigation of MHD effects on Al2O3–water nanofluid flow and heat transfer in a semi-annulus enclosure using LBM, *Energy*, Vol. 60, pp. 501-510, 2013.

[36] A. Siddiqui, M. Sheikholeslami, TiO 2-water nanofluid in a porous channel under the effects of an inclined magnetic field and variable thermal conductivity, *Applied Mathematics and Mechanics*, Vol. 39, pp. 1201-1216, 2018.

[37] T. Maranna, U. S. Mahabaleshwar, M. I. Kopp, The Impact of Marangoni Convection and Radiation on Flow of Ternary Nanofluid in a Porous Medium with Mass Transpiration, *Journal of Applied and Computational Mechanics*, Vol. 9, No. 2, pp. 487-497, 2023.

[38] M. Z. Swalmeh, F. A. Alwawi, A. Altawallbeh, K. Naganthran, I. Hashim, On the optimized energy transport rate of magnetized micropolar fluid via ternary hybrid ferro-nanosolids: A numerical report, *Heliyon*, Vol. 9, No. 12, 2023.

[39] G. R. Rajput, B. P. Jadhav, V. S. Patil, S. Salunkhe, Effects of nonlinear thermal radiation over magnetized stagnation point flow of Williamson fluid in porous media driven by stretching sheet, *Heat Transfer*, Vol. 50, No. 3, pp. 2543-2557, 2021.

[40] E. R. El-Zahar, A. Algelany, A. M. Rashad, Sinusoidal natural convective flow of non-newtonian nanoliquid over a radiative vertical plate in a saturated porous medium, *IEEE Access*, Vol. 8, pp. 136131-136140, 2020.

[41] E. R. EL-Zahar, A. M. Rashad, L. F. Seddek, The impact of sinusoidal surface temperature on the natural convective flow of a ferrofluid along a vertical plate, *Mathematics*, Vol. 7, No. 11, pp. 1014, 2019.

[42] E. El-Zahar, A. Rashad, W. Saad, L. Seddek, Magneto-hybrid nanofluids flow via mixed convection past a radiative circular cylinder, *Scientific Reports*, Vol. 10, No. 1, pp. 10494, 2020.

[43] J. Merkin, Free convection boundary layer on an isothermal horizontal cylinder, in *Heat Transfer Conference*, St. Louis, Mo., 1976, pp. ASME 5 p.

[44] M. M. Molla, M. A. Hossain, M. C. Paul, Natural convection flow from an isothermal horizontal circular cylinder in presence of heat generation, *International Journal of Engineering Science*, Vol. 44, No. 13-14, pp. 949-958, 2006.